

**Shock compression of vanadium at extremes: Theory and experiment**Philippe F. Weck<sup>1,\*</sup>, Patricia E. Kalita,<sup>1</sup> Tommy Ao,<sup>1</sup> Scott D. Crockett,<sup>2</sup> Seth Root,<sup>1</sup> and Kyle R. Cochrane<sup>1</sup><sup>1</sup>*Sandia National Laboratories, Albuquerque, New Mexico 87185, USA*<sup>2</sup>*Los Alamos National Laboratory, Los Alamos, New Mexico 87545, USA* (Received 23 May 2020; revised 25 September 2020; accepted 3 November 2020; published 16 November 2020)

The equation of state (EOS) and shock compression of bulk vanadium were investigated using canonical *ab initio* molecular dynamic simulations, with experimental validation to 865 GPa from shock data collected at Sandia's Z Pulsed Power Facility. In simulations the phase space was sampled along isotherms ranging from 3000 K to 50 000 K, for densities between  $\rho = 3$  and 15 g/cm<sup>3</sup>, with a focus on the liquid regime and the body-centered-cubic phase in the vicinity of the melting limit. The principal Hugoniot predicted from first principles is overall consistent with shock data, while it showed that current multiphase SESAME-type EOS for vanadium needed revision in the liquid regime. A more accurate SESAME EOS was developed using constraints from experiments and simulations. This work emphasizes the need to use a combined theoretical and experimental approach to develop high-fidelity EOS models for extreme conditions.

DOI: [10.1103/PhysRevB.102.184109](https://doi.org/10.1103/PhysRevB.102.184109)**I. INTRODUCTION**

Unraveling the structure-property relationship of elemental metals subjected to high-pressure (HP) and high-temperature (HT) conditions is of fundamental importance in the field of condensed matter physics, with numerous technological applications. In comparison to other elemental metals crystallizing in the high-symmetry face-centered-cubic (FCC) or hexagonal close packed (HCP) structures, body-centered-cubic (BCC) metals under extreme conditions have traditionally received less theoretical and experimental attention owing to their very high stability [1]. For example, among naturally occurring metals of Group VB (V, Nb, and Ta), the stability of the BCC structure had long been thought to be high, with no evidence of pressure-induced phase transitions found in room-temperature compression experiments of BCC V and Nb to 154 and 145 GPa [2,3] or in shock-compression experiments of BCC Ta from ambient pressure to  $\approx 300$  GPa [4].

Following the theoretical predictions of transverse acoustic phonon mode softening and anomalous behavior of the shear elastic constant  $C_{44}$  in compressed BCC vanadium [5–7], a room-temperature BCC  $\rightarrow$  rhombohedral (Rh) phase transition in vanadium was observed at  $\sim 63$ –69 GPa by synchrotron x-ray diffraction (XRD) experiments using a diamond anvil cell (DAC) to 155 GPa [8]. This phase transition originates from a complex combination of intraband Fermi surface nesting (Kohn anomaly), band Jahn-Teller effect and electronic topological transition. It was actually shown by first-principles calculations to consist of a sequence of phase transformations, i.e., BCC  $\rightarrow$  Rh1  $\rightarrow$  Rh2  $\rightarrow$  BCC, where the low-symmetry Rh1 and Rh2 phases become stable above 84 and 120 GPa, respectively, with a final reversal to BCC beyond 280 GPa

[9,10]. Additional studies have since confirmed the existence of such transitions, although inconsistency remains in the transition pressure values, depending on whether hydrostatic or nonhydrostatic conditions are used in experiments or calculations [11–21]. This discovery has challenged the conventional *s-d* electronic transition mechanism, which is regarded as the main driving force behind pressure-induced phase transitions in elemental metals. It has also renewed interest in the phase-diagram investigation of other Group VB elements [4,13,22,23].

In contrast to this wealth of information on the compressed solid phases of vanadium, limited research has been devoted to liquid vanadium under HP-HT conditions. As recently noted by Errandonea *et al.* [21], this stems in part from the scarcity of results on vanadium melting, with only few melting point calculations existing above ambient pressure [21,24], and large differences observed between melting temperatures measured from laser-heated DAC and shock-wave (SW) experiments [21,25,26]. The latest melting curve results and associated Simon-Glatzel (S-G) fit [21] provided a reasonable compromise between the considerably higher SW experiments [26] and the lower previous DAC data [25], thus contributing to improve our understanding of the vanadium equation of state (EOS) in the *P-T* range probed by experiments. SW experiments are particularly well suited for investigating extreme states of matter. The highest compression of V was achieved in the SW experiments of Al'tshuler *et al.* [27] ( $P = 338.9$  GPa) and Gathers [28] ( $P = 336.78$  GPa). The SW experiments of McQueen *et al.* [29], Dai *et al.* [26], and Foster *et al.* [30] reached pressures of 125.0, 250.1, and 74.4 GPa, respectively, along the principal Hugoniot of vanadium. However, the lack of experimental shock data and computational predictions at HP-HT conditions beyond shock melting has hampered development of a reliable tabulated EOS for vanadium in this regime [31].

\*pfweck@sandia.gov

In this work, the EOS and shock compression of bulk vanadium were investigated within the framework of density-functional theory (DFT) with Mermin's generalization to finite temperature, with experimental validation to 865 GPa from shock data collected at Sandia's Z Pulsed Power Facility. Previous studies have shown the importance of such high-fidelity *ab initio* simulations to correctly analyze high-pressure experiments [21,23,32–37]. The principal Hugoniot of vanadium was predicted from canonical *ab initio* molecular dynamics (AIMD) simulations by solving the Rankine-Hugoniot relations, and was validated by comparison with *Z*-machine shock compression data. In simulations the phase space was sampled along isotherms in the range 3000–50 000 K, for densities between  $\rho = 3$  and 15 g/cm<sup>3</sup>, with a focus on the liquid regime and the body-centered-cubic phase in the vicinity of the melting limit. AIMD predictions were also compared with existing shock data [26–30,38] and results from the current multiphase SESAME 2552 EOS for vanadium [31,39]. A revised multiphase SESAME 2553 EOS was developed using constraints from experiments and simulations.

The computational and experimental methods utilized in this study are described in Sec. II, followed by a discussion of our results in Sec. III. Our findings and conclusion are summarized in Sec. IV.

## II. METHODS

### A. Density-functional theory calculations

First-principles spin-polarized DFT calculations (at 0 K) were conducted using the Vienna *ab initio* simulation package (VASP) [40] within the generalized gradient approximation (GGA) [41], with the parametrization of Perdew, Burke, and Ernzerhof (PBE) [42] to compute the exchange-correlation energy. This functional was successfully used in previous studies to predict the EOS and phase boundaries of vanadium [19,21] and other elemental metals [23,36]. Similarly to previous DFT/AIMD studies of vanadium [19,21], the projector augmented wave (PAW) method [43,44] was utilized to describe the interaction between the 13 valence electrons of V (*3s*, *3p*, *3d*, *4s*) and its ionic core. In the Kohn-Sham (KS) equations, the outer V electrons were treated as valence states, while the remaining core electrons and nuclei were represented by a PAW pseudopotential [*s* semicore states were treated as valence states (*sv*) in the V PAW potential]. The KS equations were solved using the special Davidson block iteration matrix diagonalization scheme [45]. The plane-wave cutoff energy for the electronic wave functions was set to 700 eV, ensuring convergence of the system total energy to better than 1 meV/atom. The Methfessel-Paxton scheme [46] was utilized to control partial occupancies for each wave function. Bulk vanadium was represented using a BCC periodic unit cell (space group *Im* $\bar{3}m$ , IT No. 229, *Z* = 2) and ionic and cell relaxations were carried out simultaneously, without symmetry constraints applied, with a convergence tolerance set to 0.01 eV/Å for the Hellmann-Feynman forces acting on atoms. The Brillouin zone (BZ) was sampled using the Monkhorst-Pack *k*-point scheme [47] with a 11×11×11 *k*-point mesh.

### B. *Ab initio* molecular dynamics simulations

AIMD simulations were conducted with VASP at the GGA/PBE level of theory using spin-polarized DFT with Mermin's generalization of the KS equations to finite temperature [48] (Mermin-Kohn-Sham equations). Simulations were conducted in the canonical (NVT) ensemble along isotherms ranging from 3000 to 50 000 K and densities from 3.0 to 15.0 g/cm<sup>3</sup>. In all AIMD simulations, large 128-atom 4×4×4 vanadium periodic supercells were utilized to ensure negligible interaction between the structures simulated and their periodic images. Property averaging in the BZ was carried out using the Baldereschi's mean-value special *k* point [49]. A time step for ion-motion of 0.8 fs was used in the simulations, with velocities scaled to the temperature at each simulation step. Each NVT simulation was run for typically  $\simeq 5$ –10 ps. Equilibration was considered achieved when the block average [50] of the standard deviation of the pressure was less than  $\simeq 0.5\%$ .

The principal Hugoniot for bulk vanadium was calculated from AIMD simulations using the Rankine-Hugoniot jump conditions [51]. The Hugoniot consists of the locus of (*P*, *V*, *T*) points that satisfy the Hugoniot relation [51],

$$E - E_0 + (1/2)(P + P_0)(V - V_0) = 0, \quad (1)$$

where *E* is the specific internal energy, *P* is the pressure,  $V = 1/\rho$  is the specific volume of shocked bulk vanadium, and *E*<sub>0</sub> and *P*<sub>0</sub> are the reference energy and pressure computed from AIMD simulations at 300 K for the fully dense vanadium BCC structure. The BCC structure observed experimentally under ambient temperature and pressure conditions [52,53] was selected as a reference, with an equilibrium lattice parameter of  $a_0 = 3.0274 \pm 0.0001$  Å, corresponding to an initial volume per atom of  $V_0 = 13.873$  Å<sup>3</sup> and a theoretical material density (TMD) of  $\rho_0 = 6.097$  g/cm<sup>3</sup>. Hugoniot states were obtained by running NVT simulations at multiple temperatures between 3000 and 50 000 K, for several isotropically compressed specific volumes from ambient to elevated pressure. Each Hugoniot state was obtained by interpolating the (*P*, *T*) points which bracket the Hugoniot temperature and pressure for each specific volume. In order to calculate the Hugoniot of porous vanadium, the full-density volume *V*<sub>0</sub> in Eq. (1) was substituted with the initial porous volume  $V_{00} = 1/\rho_{00}$ , while the reference energy *E*<sub>0</sub> and pressure *P*<sub>0</sub> of full-density vanadium at ambient conditions were conserved in the Hugoniot relation.

### C. SESAME equation of state

The original SESAME 2552 EOS for vanadium was found to have deficiencies in the high-pressure liquid regime. A new EOS table, SESAME 2553 was developed as a result of the work presented in this paper. SESAME 2553 is based on the 2552 table with two changes made to improve the EOS fit in the liquid regime.

The standard division of the Helmholtz free energy was used to divide the energy into three terms: cold curve, ion thermal, and electron thermal components, i.e.,

$$F(T, V) = E_{\text{cold}} + F_{\text{ion}}(T, V) + F_{\text{electron}}(T, V). \quad (2)$$

The ion thermal component used a standard Debye model, which incorporates a Lindemann melt curve. The ambient pressure melting temperature was set to match the one-atmosphere melt temperature and density from isobaric expansion data [54]. The variation of the Grüneisen gamma parameter with density was obtained by matching the intersection of the Hugoniot with the melt curve to produce the correct transition pressure and density from sound speed measurements. The electron thermal component was determined using the Thomas-Fermi-Dirac (TFD) model. A complete description of the 2552 EOS model is found in Ref. [31].

The differences between 2552 and 2553 come from two parameters. For 2552, the cold curve was determined using a Mie-Grüneisen approximation to the Hugoniot data from the LASL shock data handbook [38] and setting the Grüneisen gamma parameter to 1.5 at room temperature. A compression math point was used to interpolate the cold curve into the zero-temperature TFD region. For table 2553, however, the cold curve was optimized to match the DFT simulations of this work and Rudin [55]. While 2552 used a Vinet EOS fit to the cold curve, 2553 uses a Birch-Murnaghan EOS fit. This switch allowed for better fitting to match the AIMD and experimental shock data.

The second change between 2553 and 2552 is in the logarithmic derivative of the Grüneisen gamma with respect to the density:

$$d\Gamma = \frac{\partial \ln(\Gamma)}{\partial \ln(\rho)}. \quad (3)$$

The quantity  $d\Gamma$  affects the thermal response of the ion thermal contribution to the EOS. Reducing this parameter increases the thermal response of the ionic thermal contribution to the EOS—the temperature increases more with increasing pressure. The adjustment of  $d\Gamma$  in the solid region improved the data match in the liquid region. The liquid model was then approximated from the solid model using an estimate of the change in entropy for melt at constant pressure [56].

#### D. Experimental methods

We carried out shock compression experiments using the Sandia Z-machine [57]. The Z-machine is a pulsed power facility capable of producing shaped current pulses and induced magnetic fields more than 20 MA and 10 MG, respectively. The combined current and magnetic field densities generate magnetic pressures to  $\sim 870$  GPa in the present experiments. In general aluminum flyer plates can be accelerated up to 40 km/s [58]. An Al flyer plate is shocklessly accelerated toward the target stack as shown in Fig. 1(a). The stack is composed of a sample of vanadium ( $\sim 500 \mu\text{m}$ ,  $\rho_0 = 6.097 \text{ g/cm}^3$ ) and a TPX window. Although the back side of the flyer is melted by the high current, the impact side of the flyer remains at solid density [58]. Impact produces a steady shock in the V sample. A velocity interferometer system for any reflector (VISAR [59,60]) measures the flyer plate velocity ( $V_F$ ) up to impact at the target [Fig. 1(b)]. Since the V sample is opaque to VISAR light, impact time is determined from fiducials observed in the transparent windows both above and below the V sample. Impact time on V is determined from those fiducials and is then corrected for any measured tilt of

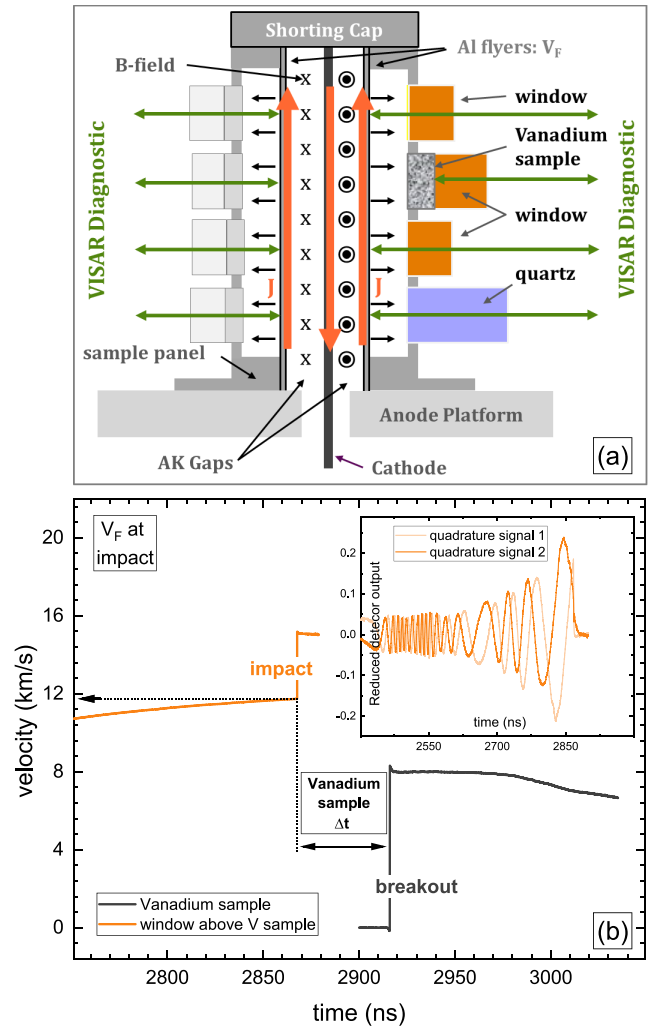


FIG. 1. (a) The experimental Z sample panel and flyer configuration. (b) Representative VISAR signal showing the measurement of impact and breakout time and the quartz witness measurement.

the impact plane and for the relative offset of the 2 windows and the V sample (typically a few  $\mu\text{m}$ ). Shock breakout is directly monitored at the V back surface, through a window. We then calculate the V shock velocity ( $U_s$ ) using the transit time determined from the VISAR fiducials and the measured thickness. The shock wave is also monitored in a thick quartz witness window, which allows us to determine any correction due to acceleration of the flyer and apply this correction to the  $V U_s$ .

In our experiments we use two, push-pull VISAR systems with dual velocity per fringe (VPF) capabilities. Three VISAR signals were recorded for the V sample eliminating  $2\pi$  ambiguities and providing redundant measurements for improved precision. We recorded three different VPFs on the sample: 0.5878 km/s/f, 1.0632 km/s/f, and 1.4317 km/s/f. For the transit time measurements, the uncertainty was less than 0.5%. In the VISAR analysis, we use a transit time determination of the shock velocity using unprocessed VISAR signals. The inset of Fig. 1(b) shows one quadrature from an unprocessed VISAR signal. To calculate transit time, we determine when the raw VISAR signal has a change larger than the standard

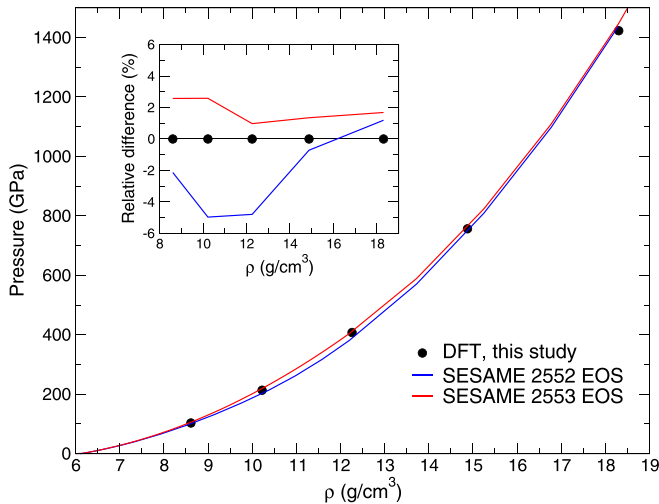


FIG. 2. Variation of the pressure as a function of density for BCC vanadium calculated from DFT at the athermal limit. The zero-temperature compression curves (cold curves) predicted using the SESAME 2552 and 2553 EOSs are displayed for comparison. The relative differences between SESAME EOSs and DFT results, used as reference values, are shown in the inset.

deviation of the signal prior to the change. That marks our impact and our transit into the backing TPX window. We use the standard deviation from the transit time determination, along with the uncertainty in the sample thickness to give the error in the shock velocity.

### III. RESULTS AND DISCUSSION

#### A. DFT modeling at $T = 0$ K

The relaxed unit-cell lattice parameter of BCC vanadium bulk is  $2.998 \text{ \AA}$  ( $V_0 = 13.473 \text{ \AA}^3/\text{atom}$ ,  $\rho_0 = 6.278 \text{ g/cm}^3$ ) using the sv PAW pseudopotential (13 valence electrons). For comparison, relaxation calculations using the pv PAW pseudopotential (11 valence electrons) and the sv\_GW PAW pseudopotential (13 valence electrons) yielded  $2.997 \text{ \AA}$  ( $V_0 = 13.460 \text{ \AA}^3/\text{atom}$ ,  $\rho_0 = 6.285 \text{ g/cm}^3$ ) and  $2.994 \text{ \AA}$  ( $V_0 = 13.419 \text{ \AA}^3/\text{atom}$ ,  $\rho_0 = 6.304 \text{ g/cm}^3$ ), respectively. The lattice parameter obtained with the sv PAW pseudopotential is in closer agreement with the room-temperature measurements of  $a_0 = 3.0274 \pm 0.0001 \text{ \AA}$  ( $V_0 = 13.873 \text{ \AA}^3/\text{atom}$ ,  $\rho_0 = 6.097 \text{ g/cm}^3$ ) by Roldan *et al.* [52] for 99.5% pure vanadium powder and  $a_0 = 3.026 \text{ \AA}$  ( $V_0 = 13.861 \text{ \AA}^3/\text{atom}$ ,  $\rho_0 = 6.104 \text{ g/cm}^3$ ) by Yu *et al.* [17] for 99.93% pure vanadium samples. These DFT predictions are in line with the values of  $2.99\text{--}3.00 \text{ \AA}$  obtained by Han *et al.* with DFT PWSCF and all-electron FLAPW calculations [61].

The  $P$ - $V$  variation of BCC vanadium bulk calculated in this study from DFT at the athermal limit is shown in Fig. 2, along with the cold curves predicted using the SESAME 2552 and 2553 EOSs for vanadium. The DFT cold curve is in overall excellent agreement with the results from the SESAME 2552 and 2553 EOS predictions, with relative differences of less than 5% and 3%, respectively (see inset in Fig. 2). Therefore, any discrepancies observed between the EOS/Hugoniot computed at finite temperature from AIMD

simulations and predicted from the SESAME 2552 and 2553 EOSs can be ascribed essentially to differences between thermal ionic or electronic contributions in AIMD simulations and in the SESAME EOSs.

#### B. Equation of state and shock Hugoniot

##### 1. Experimental Hugoniot state

The experimentally measured Hugoniot data for V are listed in Table I. Knowing the initial densities of the V and the Al flyer plate and measuring the  $V_F$  and the vanadium  $U_s$ , we calculated the V Hugoniot state density, pressure, and particle velocity ( $u_p$ ). The Hugoniot state was determined using a Monte Carlo impedance matching analysis [62,63] to solve the Rankine-Hugoniot equations [51]. The Monte Carlo impedance matching (MCIM) method accounts for the correlated and uncorrelated uncertainties in the experimental measurement and the Al Hugoniot standard. In the MCIM, uncorrelated random numbers with one standard deviation equal to the measurement uncertainty were used to adjust the flyer velocity, the shock velocity, and the initial densities about their mean value. Correlated random numbers adjust the fit parameters to the aluminum Hugoniot standard. The linear fit parameters and correlation between the parameters for the aluminum standard is listed in Table II. The impedance calculation was performed to get  $u_p$ ,  $\rho$ , and  $P$  in the Hugoniot state. The data were saved and the calculation restarted using new random numbers. A database of Hugoniot states was built during  $10^7$  iterations and the final Hugoniot state was calculated as the mean with 1-standard deviation of the distribution as the uncertainty.

##### 2. *Ab initio* molecular dynamics simulations

To test the accuracy of the AIMD simulations conducted in this study, initial simulations were run at ambient conditions and in the liquid state near the melting point. Figure 3 shows the radial pair distribution function (RDF),  $g(r)$ , of vanadium computed from AIMD simulations at 300 K (BCC phase,  $\rho = 6.097 \text{ g/cm}^3$ ) and 2200 K (liquid,  $\rho = 5.350 \text{ g/cm}^3$ ). The predicted structure of liquid vanadium at 2200 K qualitatively agrees with the RDF measurement of Waseda [64] at 2173 K and  $\rho = 5.355 \text{ g/cm}^3$ , although the calculated RDF is slightly shifted to shorter distances compared to experiment. As expected,  $g(r)$  of liquid vanadium exhibits short-range order, with a smaller number of peaks at short distance in the RDF compared to the simulated  $g(r)$  of BCC-structured vanadium at 300 K, and steady oscillatory decay to a constant value at large  $r$ .

The reference energy and pressure of  $E_0 = -8.952 \pm 0.005 \text{ eV/atom}$  and  $P_0 = -3.69 \pm 0.14 \text{ GPa}$  were obtained from AIMD simulations at 300 K for the full-density V BCC structure ( $\rho = 6.097 \text{ g/cm}^3$ ).

The variations of the specific internal energy and pressure of vanadium as a function of density computed from AIMD simulations along isotherms between 3000 and 50 000 K are displayed in Figs. 4 and 5, respectively. The lowest isotherm was chosen at 3000 K since it is slightly above the temperature of the BCC-rhombohedral phase boundary located below 2000 K, with the Rh1/Rh2 phase domain covering the

TABLE I. Experimental data for the principal Hugoniot of vanadium.

Shot	Impactor	Flyer velocity (km/s)	$u_p$ (km/s)	$U_s$ (km/s)	$\rho$ (g/cm <sup>3</sup> )	Pressure (GPa)
Z3427	Al	10.93 ± 0.01	4.16 ± 0.03	10.38 ± 0.09	10.17 ± 0.11	263 ± 2
Z3396	Al	11.72 ± 0.02	4.45 ± 0.03	10.85 ± 0.06	10.34 ± 0.09	294 ± 2
Z3391	Al	13.59 ± 0.02	5.20 ± 0.04	11.65 ± 0.10	11.01 ± 0.13	370 ± 3
Z3441	Al	22.64 ± 0.02	8.67 ± 0.07	16.37 ± 0.18	12.97 ± 0.25	866 ± 7

pressure range  $\sim 60$ – $280$  GPa [8,19,21]. The melting points calculated from the Simon-Glatzel fit to the melting results of Ref. [21] are also shown in Fig. 5. This S-G melting curve, i.e.,  $T_m(K) = 2183 \times [1 + (P/32)]^{0.46}$ , was selected in this study as it provides a reasonable compromise between the considerably higher SW experiments [26] and the lower previous DAC data [25].

Using the variations of the specific internal energy and pressure of vanadium as functions of density shown in Figs. 4 and 5, the sound speed was calculated as a function of density for temperatures in the range 3000–50 000 K (see Fig. 6). The bulk sound speed was computed as:

$$C_s = \sqrt{\left. \frac{\partial P}{\partial \rho} \right|_s} = \left[ \left. \frac{\partial P}{\partial \rho} \right|_T + \frac{\left( \left. \frac{\partial P}{\partial T} \right|_\rho \right)^2}{\rho^2 \left. \frac{\partial E}{\partial T} \right|_\rho} T \right]^{\frac{1}{2}}. \quad (4)$$

The results show that sound speed increases as temperature increases and as density increases. The sound speeds for the lowest isotherms of vanadium are slightly larger than the value of  $4.742 \pm 0.084$  km/s measured [65] at the melting temperature of  $T_m = 2163$  K; from the experimental characterization of liquid vanadium [64], the density of liquid vanadium at 2173 K [64] is  $\rho \simeq 5.35$  g/cm<sup>3</sup>. At room temperature and atmospheric pressure, the bulk sound speed of full-density BCC vanadium ( $\rho_0 \simeq 6.104$  g/cm<sup>3</sup>) was recently measured to be  $5.139 \pm 0.018$  km/s using a pulse-echo technique [17]. Sound speed in liquids is dependent on the density of the liquid, which in turn is dependent on temperature, so the speed of sound in liquids also varies with temperature. The range of sound speeds represented in Fig. 6 also appears consistent with sound speeds measured by Dai *et al.* along the V principal Hugoniot, which vary between 8.62 to 10.00 km/s from 154 and 250 GPa [26].

Using in Eq. (1) the reference energy  $E_0$  and pressure  $P_0$  computed from AIMD simulations at 300 K for full-density BCC vanadium, the principal Hugoniot was obtained by interpolating  $(P, T)$  points which bracket the Hugoniot temperature and pressure for each specific volume. The  $P$ - $\rho$  relationship along the principal Hugoniot of vanadium ( $\rho_0 = 6.097$  g/cm<sup>3</sup>) calculated from AIMD simulations is shown in Fig. 7, along with the Hugoniot data obtained from Z-machine

TABLE II. Linear fit parameters and the off-diagonal term in the covariance matrix for the fit parameters of the Al flyer.  $U_s = C_0 + S_1 u_p$ .

Flyer	$C_0$ (km/s)	$S_1$	$\sigma_{C_0} \sigma_{S_1} \times 10^3$
Al	$6.322 \pm 0.231$	$1.188 \pm 0.020$	$-4.605$

and from previous experimental investigations [26–30,38] and with the predictions from the vanadium SESAME 2552 and 2553 EOS tables [31,39]. The pressure values calculated from AIMD along the principal Hugoniot reproduce within  $\sim 1$ – $4\%$  the values of  $263 \pm 2$ ,  $294 \pm 2$ , and  $866 \pm 7$  GPa measured using the Z-machine (see Table I), with AIMD predictions remaining nearly within experimental density error bars (see Fig. 7). The largest pressure discrepancy between AIMD and Z-machine measurements is  $\sim 7\%$  for  $370 \pm 3$  GPa at  $\rho = 11.01$  g/cm<sup>3</sup>. Both Z-machine data and AIMD results appear stiffer than the tabulated SESAME 2552 Hugoniot and most previous SW data utilized to develop the SESAME 2552 EOS. The SESAME 2553 Hugoniot is also significantly stiffer than its SESAME 2552 predecessor and in overall closer agreement with Z-machine data. It is worth noting that the data for the previous highest compression of V achieved in the SW experiments of Al'tshuler *et al.* [27] ( $P = 338.9$  GPa,  $\rho = 10.75$  g/cm<sup>3</sup>) and Gathers [28] ( $P = 336.78 \pm 1.69$  GPa,  $\rho = 10.751 \pm 0.064$  g/cm<sup>3</sup>) are in close agreement with the present Z-machine data and AIMD results. The SW data of Dai *et al.* [26], as well as the lowest pressure data of Al'tshuler *et al.* and Gathers, are consistently softer than the AIMD predictions. For comparison, the SW data of Foster *et al.* [30] and the historical explosive drive data from the LASL compendium compiled by Marsh [38] based on the measurements of McQueen *et al.* [29] are also displayed in Fig. 7, although

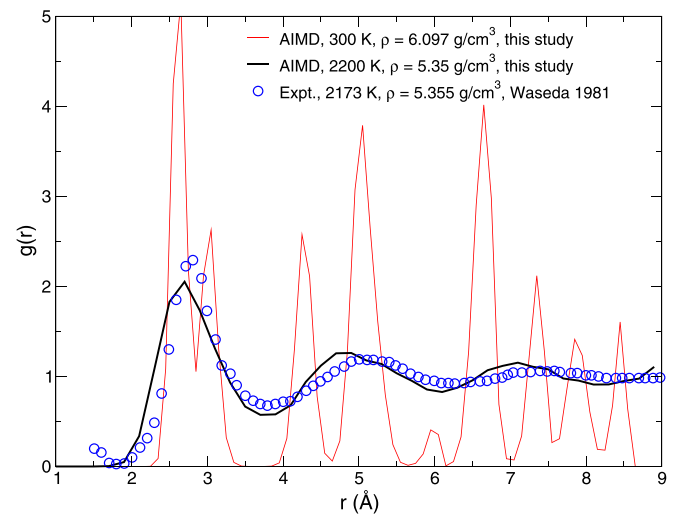


FIG. 3. Radial pair distribution function,  $g(r)$ , of vanadium calculated from AIMD simulations at 300 K (BCC phase,  $\rho = 6.097$  g/cm<sup>3</sup>) and 2200 K (liquid,  $\rho = 5.350$  g/cm<sup>3</sup>). The structure of liquid vanadium measured at 2173 K and  $\rho = 5.355$  g/cm<sup>3</sup> [64] is also shown for comparison.

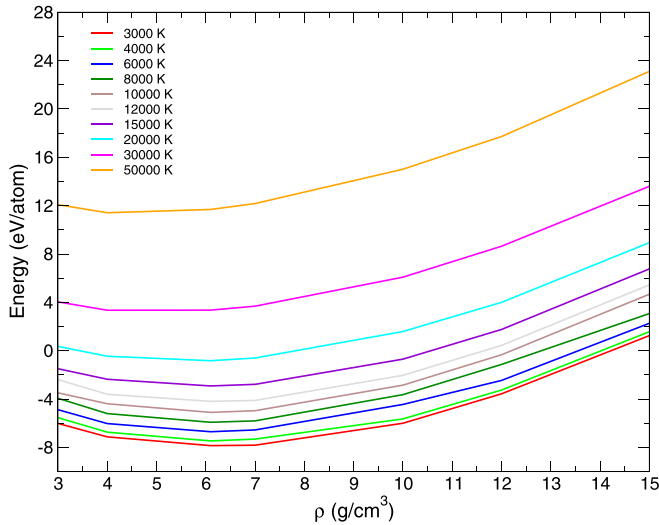


FIG. 4. Variation of the specific internal energy of vanadium as a function of density calculated from AIMD simulations along isotherms in the range 3000–50 000 K.

they focus essentially on the lower pressure range for the BCC and rhombohedral phases of V and have thus limited overlap with the present results.

The largest differences between AIMD and SESAME 2552 Hugoniot occur at HP-HT conditions beyond shock melting, where the lack of experimental SW data and computational predictions has hampered development of a reliable tabulated V EOS in this regime [31]. As discussed in Sec. III A, since the cold curve contribution to the SESAME 2552 EOS is overall similar to that of the present first-principles calculations, it can be inferred that most of the discrepancies between the Hugoniot curves obtained from AIMD simulations and the SESAME 2552 EOS under HP-HT conditions originate from differences between thermal ionic or electronic contributions

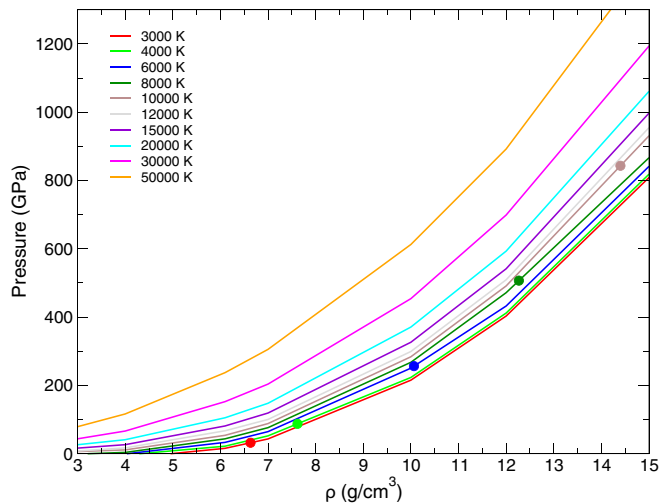


FIG. 5. Variation of the pressure as a function of density for vanadium calculated from AIMD simulations along isotherms in the range 3000–50 000 K. Melting points calculated from the Simon-Glatzel (S-G) fit to the melting results of Ref. [21] are indicated by solid circles on isotherms.

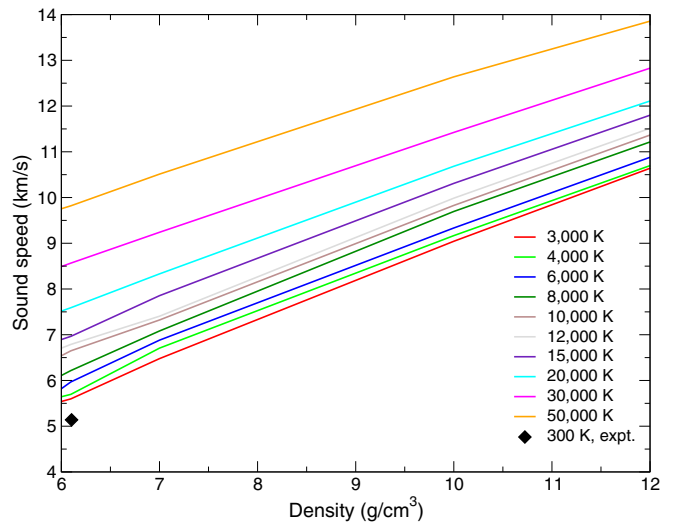


FIG. 6. Variation of the sound speed for vanadium as a function of density, along isotherms between 3000 and 50 000 K. The experimental ambient condition sound speed for full density V [17] is shown for comparison.

in both modeling approaches. In particular, the thermal ionic contribution to SESAME 2552 EOS was developed using a standard Debye model, which incorporates Lindemann melting, with parameters selected to reproduce the data of Gathers [28] and Dai *et al.* [26], i.e., the best data available when SESAME 2552 EOS was built. The recent reexamination of the melting curve and phase diagram of V by Errandonea *et al.* [21] questioned the accuracy of temperatures determined by Dai *et al.* using a gray-body fit to radiance measurements at discrete wavelengths [26]. Such findings might explain in part the large discrepancies observed between melting temperatures measured from laser-heated DAC and SW experiments [21,25,26]. Remaining discrepancies might be ascribed to

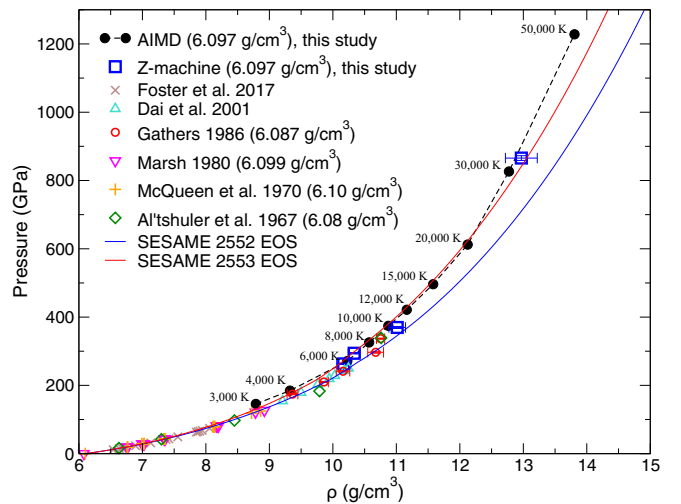


FIG. 7.  $P$ - $\rho$  relationship along the principal Hugoniot of vanadium ( $\rho_0 = 6.097 \text{ g/cm}^3$ ) calculated from AIMD simulations. Principal Hugoniot data obtained from Z-machine and previous experimental studies [26–30,38] are represented, along with predictions from the vanadium SESAME 2552 and 2553 EOS tables [31,39].

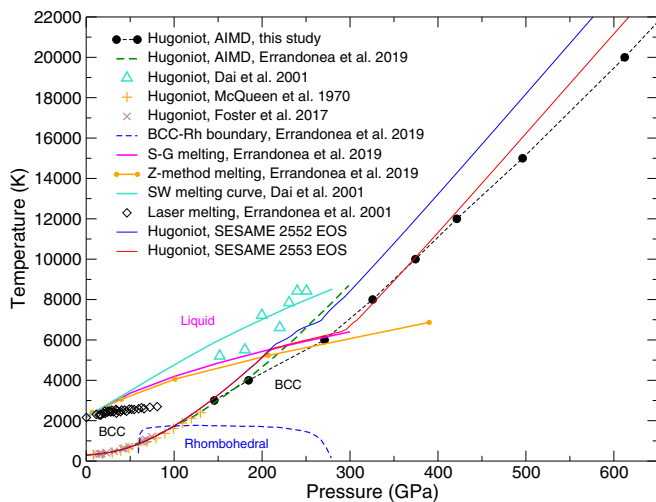


FIG. 8.  $P$ - $T$  phase diagram of vanadium. The principal Hugoniot of vanadium ( $\rho_0 = 6.097$  g/cm<sup>3</sup>) calculated in this study from AIMD simulations is represented, along with previous computational results [21]. Principal Hugoniot data from previous experimental studies [26–30,38] are represented, along with predictions from the vanadium SESAME 2552 and 2553 EOS tables [31,39]. The BCC-Rh phase boundary [21] and melting curve estimates are also shown [21,25,26].

differences in V compressibility under quasistatic laser-heated DAC and highly nonhydrostatic SW conditions [21]. The new parameters used in the development of the SESAME 2553 EOS appear to noticeably improve the description of the thermal ionic or electronic contributions at high temperature compared to the SESAME 2552 EOS, as shown by the closer agreement between SESAME 2553 Hugoniot states and Z-machine data.

Figure 8 represents the  $P$ - $T$  phase diagram of vanadium, including the principal Hugoniots calculated from AIMD simulations in this study and Ref. [21] and from previous experimental studies [26–30,38] and the SESAME 2552 and 2553 EOS tables [31,39]. The tentative BCC-Rh phase boundary shown in Fig. 8 is based on the results reported by Ding *et al.* [8], Wang *et al.* [19], and Errandonea *et al.* [21]. The various melting curves depicted correspond to the estimates determined from SW measurements by Dai *et al.* [26], and DAC measurements and Z-method calculations by Errandonea *et al.* [21,25]. As shown in Fig. 8, Hugoniot states calculated for BCC V at 3000 and 4000 K reproduce recent calculations by Errandonea *et al.* [21] within  $\sim 3\%$ , although differences appear in the liquid regime. Similarly to the Hugoniot results from the multiphase SESAME 2552 and 2553 EOSs, the present AIMD Hugoniot curve features a clear discontinuity near melting in the  $(P, T)$  representation, while no such discontinuity was predicted in previous calculations [21]. Although the accuracy of temperatures determined by Dai *et al.* might be questionable, a similar discontinuity was found in their Hugoniot data near  $\sim 225$  GPa at the onset of shock melting [26]. While the agreement between Hugoniot states calculated using the SESAME 2552 and AIMD is good at low temperature for BCC V, SESAME 2552 Hugoniot predictions tend to depart noticeably from the present AIMD results in the

HP-HT liquid regime, where fewer experimental data were available to constrain the SESAME 2552 EOS parameters [31]. The Hugoniot predictions using the SESAME 2553 EOS are nearly identical to those of the SESAME 2552 EOS up to melting, where they follow the S-G melting curve proposed by Errandonea *et al.*, while they closely match AIMD Hugoniot states in the liquid phase up to  $\sim 400$  GPa. At higher pressure, the temperature along the Hugoniot is predicted to increase faster with the SESAME 2553 EOS than in AIMD simulations. This deviation of the proposed SESAME 2553 EOS from AIMD results at high pressure is not negligible and is challenging to resolve in the EOS modeling. The determination of the model parameters used to capture the thermal response for an EOS is typically based on low pressure data such as isobaric data (thermal expansion, adiabatic bulk modulus, specific heat, and melting point data). Temperature measurements under high compression until recently have been unreliable. The optimization of the parameters used in this EOS is limited to the cold curve and ion models where the thermal electronic contribution to the free energy is minimal. EOS models such as TFD used for modeling the thermal electronic contribution can lead to uncertainties in the EOS which lead to an underestimation of the thermal response for the specific heat in intermediate regions. However, the TFD model is a reasonable approximation and converges to the correct thermal limits at high temperature and density.

According to the present AIMD Hugoniot, shock melting occurs at  $T_m = 6178$  K and  $P_m = 276$  GPa using the SG melting curve or at 5680 K and 257 GPa using the Z-method melting curve [21]. The corresponding values along the Hugoniot in Ref. [21] are  $\sim 5716$  K at  $\sim 225$  GPa and  $\sim 5330$  K at  $\sim 218$  GPa, respectively. In comparison, melting along the SESAME 2552 Hugoniot was predicted at 6022 K and 222 GPa [31], close to the estimate of 6150 K and 220 GPa by Luo *et al.* based on ultrafast dynamic experiments [66]. However, if the SG and Z-method melting curves [21] are used in conjunction with the SESAME 2552 Hugoniot, values of 5518 K at 209 GPa and 5149 K at 200 GPa are obtained, respectively. The corresponding values using the SESAME 2553 Hugoniot with these SG and Z-method melting curves are 5564 K at 213 GPa and 5167 K at 201 GPa, respectively. These results show that there is still no general consensus on accurate  $(T_m; P_m)$  values of shock melting along the principal Hugoniot of vanadium. This might stem in part from the difficulty in accurately resolving recrystallization associated with microstructure transformation immediately below melting and actual melting transition [21]. Similar microstructural transformation below melting was recently found in BCC Mo subjected to HP laser heating [67].

Based on the conservation equations, the  $u_p$  and  $U_s$  velocities were computed from the AIMD-generated table using the following expressions:

$$u_p = \sqrt{\frac{P - P_0}{\rho_0}} \sqrt{1 - \frac{\rho_0}{\rho}} \quad (5)$$

and

$$U_s = \sqrt{\frac{P - P_0}{\rho_0}} / \sqrt{1 - \frac{\rho_0}{\rho}}. \quad (6)$$

TABLE III. Hugoniot states for vanadium, with an initial solid density of  $\rho_0 = 6.097 \text{ g/cm}^3$  and a porous density of  $\rho_{00} = 5.35 \text{ g/cm}^3$ , calculated from canonical AIMD/PBE simulations along isotherms between 3000 and 50 000 K.

$T$ (K)	$\rho_0 = 6.097 \text{ g/cm}^3$				$\rho_{00} = 5.35 \text{ g/cm}^3$			
	$\rho$ ( $\text{g/cm}^3$ )	$P$ (GPa)	$u_p$ (km/s)	$U_s$ (km/s)	$\rho$ ( $\text{g/cm}^3$ )	$P$ (GPa)	$u_p$ (km/s)	$U_s$ (km/s)
3000	8.79	145.6	2.74	8.94	7.79	88.4	2.32	7.41
4000	9.32	184.7	3.27	9.45	8.16	118.0	2.80	8.13
6000	10.23	271.1	4.27	10.56	8.78	175.0	3.61	9.24
8000	10.57	325.7	4.78	11.30	9.27	221.2	4.22	9.97
10 000	10.87	374.4	5.22	11.88	9.71	264.9	4.75	10.57
12 000	11.16	421.5	5.63	12.39	10.06	305.3	5.20	11.11
15 000	11.58	496.2	6.23	13.16	10.35	364.1	5.76	11.93
20 000	12.12	612.3	7.09	14.26	10.80	459.9	6.61	13.10
30 000	12.77	826.4	8.44	16.14	11.54	642.3	8.05	15.00
50 000	13.81	1228.2	10.62	19.02	12.44	973.8	10.20	17.91

The Hugoniot states in  $(u_p, U_s)$  and  $(\rho, P)$  spaces for vanadium, with an initial solid density of  $\rho_0 = 6.097 \text{ g/cm}^3$  and a porous density of  $\rho_{00} = 5.35 \text{ g/cm}^3$  (88% of TMD), calculated from canonical AIMD/PBE simulations along isotherms between 3000 and 50 000 K are summarized in Table III. This initial porosity value was chosen since it is a typical value of plasma-sprayed vanadium used in various coating applications [68]. Figure 9 shows the computed variations of  $U_s$  as a function of  $u_p$  along the Hugoniot of full-density and porous V between 3000 and 50 000 K. Z-machine data, previous measurements [26–30,38], and the predictions from the vanadium SESAME 2552 and 2553 EOS tables for the principal Hugoniot [31,39] are also depicted.

AIMD results and Z-machine data along the principal Hugoniot are in good agreement with the previous high-compression of V in the SW experiments of Al'tshuler

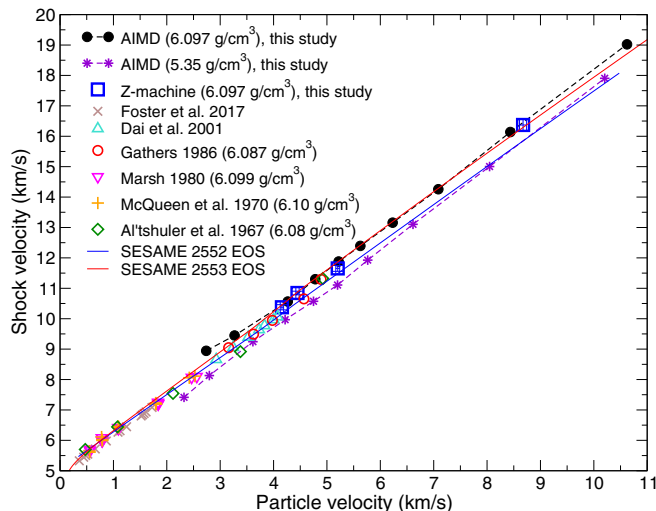


FIG. 9. Shock velocity ( $U_s$ ) versus particle velocity ( $u_p$ ) for full-density ( $\rho_0 = 6.097 \text{ g/cm}^3$ ) and porous ( $\rho_{00} = 5.35 \text{ g/cm}^3$ ) vanadium calculated from canonical AIMD simulations between 3000 and 50 000 K. Z-machine data and data from previous experimental studies [26–30,38] for full-density vanadium are represented, along with predictions from the vanadium SESAME 2552 and 2553 EOS tables [31,39].

*et al.* [27] ( $u_p = 4.92 \text{ km/s}$  and  $U_s = 11.32 \text{ km/s}$  at  $P = 338.9 \text{ GPa}$ ) and Gathers [28] ( $u_p = 4.89 \text{ km/s}$  and  $U_s = 11.29 \text{ km/s}$  at  $P = 336.78 \text{ GPa}$ ), although slightly stiffer than most previous SW ( $u_p, U_s$ ) data at lower pressure and predictions from the SESAME 2552 EOS. It is interesting to note, however, that the present AIMD predictions for the principal Hugoniot of the pure BCC phase in the  $P$ - $T$  representation at 3000 and 4000 K (see Fig. 8) are found to be in very good agreement with the previous AIMD predictions of Errandonea *et al.* [21]. Therefore, the deviation between AIMD predictions and experiments at 3000 and 4000 K in Fig. 9 might suggest that the Rh-BCC phase transition is more sluggish than shown schematically in Fig. 8 and that there might be coexistence of both phases over a broader  $P$ - $T$  domain. For this reason, the rhombohedral phase might need to be taken into account in Hugoniot calculations—up to possibly  $\sim 3000$ – $4000 \text{ K}$ —to correctly represent experimental data at lower  $P$ - $T$  conditions. The  $U_s$  vs.  $u_p$  variation obtained from the SESAME 2553 EOS is in much closer agreement with Z-machine data and AIMD than results from the SESAME 2552 EOS, with some slight departure from AIMD predictions for  $u_p \gtrsim 8 \text{ km/s}$ . Although the evolutions of  $U_s$  with  $u_p$  predicted from AIMD for TMD and porous vanadium are overall qualitatively similar, the resulting value of  $U_s$  for any given value of  $u_p$  in 12% porous V ( $\rho_{00} = 5.35 \text{ g/cm}^3$ ) is reduced by 3–10% compared to its counterpart in full-density vanadium, with the largest deviations occurring at low particle velocities in solid BCC V.

#### IV. CONCLUSION

The EOS and shock compression of vanadium were investigated using AIMD simulations between 3000 and 50 000 K for densities in the range  $\rho = 3$ – $15 \text{ g/cm}^3$ , with experimental validation using shock data from the Z-machine in the liquid regime to 865 GPa.

Very good agreement is found between principal Hugoniot results generated from AIMD simulations and Z-machine measurements collected in this study. The pressure values calculated from AIMD along the principal Hugoniot reproduce within  $\sim 1$ – $4\%$  the values of  $263 \pm 2$ ,  $294 \pm 2$ , and  $866 \pm 7 \text{ GPa}$  measured using Z-machine, with AIMD

predictions remain nearly within experimental density error bars. Both AIMD results and Z-machine data appear stiffer than the tabulated SESAME 2552 Hugoniot and most previous shock wave data utilized to develop the current SESAME 2552 EOS, although the highest compression data from the SW experiments of Al'tshuler *et al.* and Gathers are consistent with the present Z-machine data and AIMD results. The principal Hugoniot obtained from the developed SESAME 2553 EOS is significantly stiffer than its SESAME 2552 predecessor and in overall closer agreement to recent Z-machine data. According to the present AIMD Hugoniot, shock melting occurs at  $T_m = 6178$  K and  $P_m = 276$  GPa using a Simon-Glatzel fit to melting data or at 5680 K and 257 GPa using a Z-method melting curve reported recently.

The largest differences between AIMD and SESAME 2552 Hugoniots occur at HP-HT conditions beyond shock melting, where the lack of experimental SW data and computational predictions has hampered development of a reliable tabulated V EOS in this regime. Since the cold curve contribution to the SESAME 2552 EOS is overall similar to that of the present first-principles calculations, it can be inferred that most of the discrepancies between the Hugoniot curves obtained from AIMD simulations and the SESAME 2552 EOS under HP-HT conditions originate from differences between thermal ionic

or electronic contributions in both modeling approaches. In particular, the thermal ionic contribution to SESAME 2552 EOS was developed using a standard Debye model, which incorporates Lindemann melting, with parameters selected to reproduce the data of Gathers and Dai *et al.* The parameters used in the development of the SESAME 2553 EOS appear to noticeably improve the description of the thermal ionic or electronic contributions at high temperature compared to the SESAME 2552 EOS. This work emphasizes the need to use a combined theoretical and experimental approach to develop high fidelity EOS models for extreme conditions.

#### ACKNOWLEDGMENTS

Sandia National Laboratories is a multimission laboratory managed and operated by National Technology and Engineering Solutions of Sandia, LLC, a wholly owned subsidiary of Honeywell International, Inc., for the U.S. Department of Energy's National Nuclear Security Administration under Contract No. DE-NA0003525. The views expressed in the article do not necessarily represent the views of the U.S. Department of Energy or the United States Government. S.D.C. acknowledges the support of the U.S. DOE/NNSA under Contract No. DE-AC52-06NA25396.

- 
- [1] J. C. F. Millett, N. K. Bourne, N. T. Park, G. Whiteman, and G. T. Gray III, *J. Mater. Sci.* **46**, 3899 (2011).
  - [2] K. Takemura, in *Proceedings of the International Conference on High Pressure Science and Technology (AIRAPT-17)*, edited by M. H. Manghnani, W. J. Nellis, and M. F. Nicol (University Press, India, 2000), Vol. 1, p. 443.
  - [3] T. Kenichi and A. K. Singh, *Phys. Rev. B* **73**, 224119 (2006).
  - [4] M. C. Akin, J. H. Nguyen, M. A. Beckwith, R. Chau, W. P. Ambrose, O. V. Fatyanov, P. D. Asimow, and N. C. Holmes, *J. Appl. Phys.* **125**, 145903 (2019).
  - [5] N. Suzuki and M. Otani, *J. Phys.: Condens. Matter* **14**, 10869 (2002).
  - [6] A. Landa, J. Klepeis, P. Soederlind, I. Naumov, O. Velikokhatnyi, L. Vitos, and A. Ruban, *J. Phys. Chem. Solids* **67**, 2056 (2006).
  - [7] A. Landa, J. Klepeis, P. Soderlind, I. Naumov, O. Velikokhatnyi, L. Vitos, and A. Ruban, *J. Phys.: Condens. Matter* **18**, 5079 (2006).
  - [8] Y. Ding, R. Ahuja, J. Shu, P. Chow, W. Luo, and H. K. Mao, *Phys. Rev. Lett.* **98**, 085502 (2007).
  - [9] B. Lee, R. E. Rudd, J. E. Klepeis, P. Soderlind, and A. Landa, *Phys. Rev. B* **75**, 180101(R) (2007).
  - [10] B. Lee, R. E. Rudd, J. E. Klepeis, and R. Becker, *Phys. Rev. B* **77**, 134105 (2008).
  - [11] A. K. Verma and P. Modak, *Europhys. Lett.* **81**, 37003 (2007).
  - [12] W. Luo, R. Ahuja, Y. Ding, and H. K. Mao, *Proc. Natl. Acad. Sci. USA* **104**, 16428 (2007).
  - [13] L. Koči, Y. Ma, A. R. Oganov, P. Souvatzis, and R. Ahuja, *Phys. Rev. B* **77**, 214101 (2008).
  - [14] S. L. Qiu and P. M. Marcus, *J. Phys.: Condens. Matter* **20**, 275218 (2008).
  - [15] J.-H. P. Klepeis, H. Cynn, W. J. Evans, R. E. Rudd, L. H. Yang, H. P. Liermann, and W. Yang, *Phys. Rev. B* **81**, 134107 (2010).
  - [16] Zs. Jenei, H. P. Liermann, H. Cynn, J.-H. P. Klepeis, B. J. Baer, and W. J. Evans, *Phys. Rev. B* **83**, 054101 (2011).
  - [17] Y. Yu, Y. Tan, C. Dai, X. Li, Y. Li, Q. Wu, and H. Tan, *Appl. Phys. Lett.* **105**, 201910 (2014).
  - [18] D. Antonangeli, D. L. Farber, A. Bosak, C. M. Aracne, D. G. Ruddle, and M. Krisch, *Sci. Rep.* **6**, 31887 (2016).
  - [19] Y. X. Wang, Q. Wu, X. R. Chen, and H. Y. Geng, *Sci. Rep.* **6**, 32419 (2016).
  - [20] A. Landa, P. Soederlind, I. Naumov, J. Klepeis, and L. Vitos, *Computation* **6**, 29 (2018).
  - [21] D. Errandonea, S. G. MacLeod, L. Burakovsky, D. Santamaria-Perez, J. E. Proctor, H. Cynn, and M. Mezouar, *Phys. Rev. B* **100**, 094111 (2019).
  - [22] I. Papadimitriou, C. Utton, and P. Tsakirooulos, *Comput. Mater. Sci.* **107**, 116 (2015).
  - [23] P. F. Weck, J. P. Townsend, K. R. Cochrane, S. D. Crockett, and N. W. Moore, *J. Appl. Phys.* **125**, 245905 (2019).
  - [24] A. Landa, P. Söderlind, and L. H. Yang, *Phys. Rev. B* **89**, 020101(R) (2014).
  - [25] D. Errandonea, B. Schwager, R. Ditz, C. Gessmann, R. Boehler, and M. Ross, *Phys. Rev. B* **63**, 132104 (2001).
  - [26] C. Dai, X. Jin, X. Zhou, J. Liu, and J. Hu, *J. Phys. D* **34**, 3064 (2001).
  - [27] L. V. Al'tshuler, A. A. Bakanova, and I. P. Dudoladov, *Zh. Eksp. Teor. Fiz.* **53**, 1967 (1967).
  - [28] G. R. Gathers, *J. Appl. Phys.* **59**, 3291 (1986).
  - [29] R. G. McQueen, S. P. Marsh, J. W. Taylor, J. N. Fritz, and W. J. Carter, in *High Velocity Impact Phenomena*, edited by R. Kinslow (Academic Press, New York, 1970), p. 293.

- [30] J. M. Foster, A. J. Comley, G. S. Case, P. Avraam, S. D. Rothman, A. Higginbotham, E. K. R. Floyd, E. T. Gumbrell, J. J. D. Luis, D. McGonegle, N. T. Park, L. J. Peacock, C. P. Poulter, M. J. Suggit, and J. S. Wark, *J. Appl. Phys.* **122**, 025117 (2017).
- [31] S. Crockett and S. Rudin, Vanadium Equation of State (SESAME 2552): A Comparison of Old and New SESAME Tables, Los Alamos National Laboratory report, LA-UR-06-8389 (2006).
- [32] A. E. Mattsson, P. A. Schultz, M. P. Desjarlais, T. R. Mattsson, and K. Leung, *Modell. Simul. Mater. Sci. Eng.* **13**, R1 (2005).
- [33] S. Root, R. J. Magyar, J. H. Carpenter, D. L. Hanson, and T. R. Mattsson, *Phys. Rev. Lett.* **105**, 085501 (2010).
- [34] D. V. Minakov, P. R. Levashov, K. V. Khishchenko, and V. E. Fortov, *J. Appl. Phys.* **115**, 223512 (2014).
- [35] A. V. Yanilkin, *High Temp.* **55**, 40 (2017).
- [36] E. Kim, P. F. Weck, and T. R. Mattsson, *J. Appl. Phys.* **124**, 035903 (2018).
- [37] P. F. Weck, K. R. Cochrane, S. Root, J. M. D. Lane, L. Shulenburg, J. H. Carpenter, T. Sjoström, T. R. Mattsson, and T. J. Vogler, *Phys. Rev. B* **97**, 125106 (2018).
- [38] *LASL Shock Hugoniot Data*, edited by S. P. Marsh (University of California Press, Berkeley, CA, 1980), p. 658.
- [39] The SESAME EOS library is a binary, tabular compendium of equations of state for numerous materials and is maintained and disseminated by Group T-1 at the Los Alamos National Laboratory. SESAME tables are available by request through the LANL homepage at <https://www.lanl.gov/org/ddste/aldsc/theoretical/physics-chemistry-materials/sesame-database.php> or by simply performing a search at the [www.lanl.gov](http://www.lanl.gov) webpage for SESAME database.
- [40] G. Kresse and J. Furthmüller, *Phys. Rev. B* **54**, 11169 (1996).
- [41] J. P. Perdew, J. A. Chevary, S. H. Vosko, K. A. Jackson, M. R. Pederson, D. J. Singh, and C. Fiolhais, *Phys. Rev. B* **46**, 6671 (1992).
- [42] J. P. Perdew, K. Burke, and M. Ernzerhof, *Phys. Rev. Lett.* **77**, 3865 (1996).
- [43] P. E. Blöchl, *Phys. Rev. B* **50**, 17953 (1994).
- [44] G. Kresse and D. Joubert, *Phys. Rev. B* **59**, 1758 (1999).
- [45] E. R. Davidson, in *Methods in Computational Molecular Physics*, edited by G. Diercksen and S. Wilson, NATO Advanced Study Institute, Series C (Plenum, New York, 1983), Vol. 113, p. 95.
- [46] M. Methfessel and A. T. Paxton, *Phys. Rev. B* **40**, 3616 (1989).
- [47] H. J. Monkhorst and J. D. Pack, *Phys. Rev. B* **13**, 5188 (1976).
- [48] N. D. Mermin, *Phys. Rev.* **137**, A1441 (1965).
- [49] A. Baldereschi, *Phys. Rev. B* **7**, 5212 (1973).
- [50] M. P. Allen and D. J. Tildesley, *Computer Simulations of Liquids* (Oxford Science, Oxford, 1987).
- [51] *Physics of Shock Waves and High-Temperature Hydrodynamic Phenomena*, edited by Y. B. Zel'dovich and Y. P. Raizer (Dover, Mineola, NY, 2002).
- [52] M. A. Roldan, V. Lopez-Flores, M. D. Alcalá, A. Ortega, and C. Real, *J. Eur. Ceram. Soc.* **30**, 2099 (2010).
- [53] H. E. Swanson, H. F. McMurdie, M. C. Morris, E. H. Evans, and B. Paretzkin, *Standard X-ray Diffraction Powder Patterns*, Monograph 25 (National Bureau Standards, Washington DC, 1971), Section 9.
- [54] G. R. Gathers, J. W. Shaner, R. S. Hixson, and D. A. Young, *High Temp.-High Press.* **11**, 653 (1979).
- [55] S. Rudin (private communication).
- [56] E. D. Chisolm, S. D. Crockett, and D. C. Wallace, *Phys. Rev. B* **68**, 104103 (2003).
- [57] M. E. Savage, L. F. Bennett, D. E. Bliss, W. T. Clark, R. S. Coats, J. M. Elizondo, K. R. LeChien, H. C. Harjes, J. M. Lehr, J. E. Maenchen, D. H. McDaniel, M. F. Pasik, T. D. Pointon, A. C. Owen, D. B. Seidel, D. L. Smith, B. S. Stoltzfus, K. W. Struve, W. A. Stygar, L. K. Warne, J. R. Woodworth, C. W. Mendel, K. R. Prestwich, R. W. Shoup, D. L. Johnson, J. P. Corley, K. C. Hodge, T. C. Wagoner, and P. E. Wakeland, in *Proceedings of the Pulsed Power Plasma Sciences Conference* (IEEE, Los Alamitos, CA, 2007), p. 979.
- [58] R. W. Lemke, M. D. Knudson, D. E. Bliss, K. Cochrane, J.-P. Davis, A. A. Giunta, H. C. Harjes, and S. A. Slutz, *J. Appl. Phys.* **98**, 073530 (2005).
- [59] L. M. Barker and R. E. Hollenbach, *J. Appl. Phys.* **43**, 4669 (1972).
- [60] L. M. Barker and K. W. Schuler, *J. Appl. Phys.* **45**, 3692 (1974).
- [61] S. Han, L. A. Zepeda-Ruiz, G. J. Ackland, R. Car, and D. J. Srolovitz, *J. Appl. Phys.* **93**, 3328 (2003).
- [62] S. Root, K. R. Cochrane, J. H. Carpenter, and T. R. Mattsson, *Phys. Rev. B* **87**, 224102 (2013).
- [63] S. Root, L. Shulenburg, R. W. Lemke, D. H. Dolan, T. R. Mattsson, and M. P. Desjarlais, *Phys. Rev. Lett.* **115**, 198501 (2015).
- [64] Y. Waseda, *The Structure of Non-Crystalline Materials-Liquids and Amorphous Solids* (McGraw-Hill, New York, 1981).
- [65] J. Casas, N. M. Kéita, and S. G. Steinemann, *Phys. Chem. Liq. Int. J.* **14**, 155 (2003).
- [66] S.-N. Luo, T. J. Ahrens, T. Cagin, A. Strachan, W. A. I. Goddard, and D. C. Swift, *Phys. Rev. B* **68**, 134206 (2003).
- [67] R. Hrubiak, Y. Meng, and G. Shen, *Nat. Commun.* **8**, 14562 (2017).
- [68] R. E. Tokheim and A. B. Lutze, *AIP Conf. Proc.* **78**, 246 (1982).